Comparison of Ti, Zr, and Hf as Cations for Metallocene-Catalyzed Olefin Polymerization

Iñaki Silanes*, Jose M. Mercero, and Jesus M. Ugalde

Kimika Fakultatea, Euskal Herriko Unibertsitatea and Donostia International Physics Center (DIPC), P.K. 1072, 20080 Donostia, Euskadi, Spain

Received September 13, 2005

In this paper we make use of a carefully chosen counterion model, $B(CF_2Cl)_3$, for a molecularly well-defined metallocenic catalyst counterion, $B(C_6F_5)_3$, to perform a comparison of $Cp_2M(CH_3)_2$-type metallocene activities toward ethylene polymerization, for M = Ti, Zr, and Hf. Monomer complexation and chain-insertion barriers are calculated and discussed, and a higher intrinsic activity for titanium is derived. Calculations are also performed in order to add further evidence of the suitability of the counterion model used. We conclude that the model employed here can act as an accurate enough substitute for the original borate in quantum mechanical calculations.

1. Introduction

The elucidation at a molecular level of the mechanism of olefin polymerization by group 4 transition metal complexes such as metallocenes,[1−8] "constrained geometry catalyst" (CGC),[4,6,9] or other post-metallocenes[10] has attracted great interest. Despite the more than 40 years since the proposal of the most widely accepted mechanism by Cossée and Arlman,[11−15] some questions remain, and theoretical calculations on the reactive species should still be helpful to shed light on the reaction mechanism.

To model the molecular structures playing an active role in the reaction site, one would like to include in the calculations not only the catalyst cation (which bears the transition metal active site), the incoming monomer, and the growing polymer chain but also the anionic counterpart for the metal, that is, the counterion (CI). The experimentally, and industrially, most used counterion is methyl aluminoxane (MAO), which not only activates the metallocenic catalyst, making it a cation, but also regulates its affinity toward the monomer complexation, through a higher or lower degree of binding to the metal.

Unfortunately, MAO is not a molecularly well-defined species, and the substance employed in the industry is probably a mixture of different moieties.[3] A common workaround for this situation consists of substituting the MAO with a well-defined molecule that plays the same role. Such a molecule can be found among a family of boron compounds, one of which is $B(C_6F_5)_3$.

In a previous article[16] we stated that the inclusion of the full counterion species $[CH_3B(C_6F_5)_3]^-$ would increase the computational workload considerably, and thus we chose to use a smaller model for it, namely, $[CH_3B(CF_2Cl)_3]^-$. However, a recent increase of computing power has enabled us to extend the calculations to include the actual $[CH_3B(C_6F_5)_3]^-$ counterion, and so we are able to compare the results with both CIs.

The aim of the present work is to take advantage of this model to analyze the effect of the substitution of zirconium by its first- and third-row transition metal counterparts, namely, titanium and hafnium, in view of the apparent controversy raised by various interpretations of recent experiments and theoretical calculations. In this regard, some authors[3,17,18] consider Zr as the most active metallic center for a number of metallocenic or post-metallocenic olefin polymerization catalysts, while others[19,20] have found a similar activity for Zr and Ti, and yet others[21−23] reckon Ti as the most active, at least at low temperatures.

A second objective would be to gather further evidence of the suitability of our CI model as a convenient theoretical substitute for the real one.

2. Methods

Our first step is to use relatively low, although reliable enough, level quantum calculations to sketch a potential energy curve (PEC)

(1) Kawamura-Kuribayashi, H.; Koga, N.; Morokuma, K. *J. Am. Chem. Soc.* **1992**, *114*, 8687.
(2) Meier, R. J.; van Doremaele, G. H. J.; Iarlori, S.; Buda, F. *J. Am. Chem. Soc.* **1994**, *116*, 7274.
(3) Möhring, P. C.; Coville, N. J. *J. Organomet. Chem.* **1994**, *479*, 1.
(4) Woo, T. K.; Fan, L.; Ziegler, T. *Organometallics* **1994**, *13*, 2252.
(5) Brintzinger, H. H.; Fischer, D.; Mülhaupt, R.; Rieger, B.; Waymouth, R. M. *Angew. Chem., Int. Ed. Engl.* **1995**, *34*, 1143.
(6) Lanza, G.; Fragala, I. L.; Marks, T. J. *Organometallics* **2001**, *20*, 4006.
(7) Borrelli, M.; Busico, V.; Cipullo, R.; Ronca, S.; Budzelaar, P. H. M. *Macromolecules* **2003**, *36*, 8171.
(8) Yang, S.-Y.; Ziegler, T. *Organometallics* **2006**, *25* (4), 887.
(9) Lanza, G.; Fragala, I. L.; Marks, T. J. *Organometallics* **2002**, *21*, 5594.
(10) Vanka, K.; Xu, Z.; Ziegler, T. *Organometallics* **2004**, *23* (12), 2900.
(11) Cossée, P. *Tetrahedron Lett.* **1960**, *38*, 12.
(12) Cossée, P. *J. Catal.* **1964**, *3*, 80.
(13) Arlman, E. J. *J. Catal.* **1964**, *3*, 89.
(14) Arlman, E. J.; Cossée, P. *J. Catal.* **1964**, *3*, 99.
(15) Arlman, E. J. *J. Catal.* **1966**, *5*, 178.
(16) Silanes, I.; Ugalde, J. M. *Organometallics* **2005**, *24* (13), 3233.
(17) Alonso-Moreno, C.; Antiñolo, A.; López-Solera, I.; Otero, A.; Prashar, S.; Rodríguez, A. M.; Villaseñor, E. *J. Organomet. Chem.* **2002**, *656*, 129.
(18) Beckerle, K.; Capacchione, C.; Ebeling, H.; Manivannan, R.; Mülhaupt, R.; Proto, A.; Spaniol, T. P.; Okuda, J. *J. Organomet. Chem.* **2004**, *689*, 4636.
(19) Bott, R. K. J.; Hughes, D. L.; Schormann, M.; Bochmann, M.; Lancaster, S. J. *J. Organomet. Chem.* **2003**, *665*, 135.
(20) Gil, M. P.; Casagrande, O. L., Jr. *J. Organomet. Chem.* **2004**, *689*, 286.
(21) Andrés, R.; de Jesús, E.; de la Mata, F. J.; Flores, J. C.; Gómez, R. *J. Organomet. Chem.* **2005**, *690*, 939.
(22) Kaminsky, W. *Catal. Today* **1994**, *20*, 257.
(23) Kim, S.-J.; Lee, Y.-J.; Kang, E.; Kim, S. H.; Ko, J.; Cheong, B. L. M.; Suh, I.-H.; Kang, S. O. *Organometallics* **2003**, *22*, 3958.

10.1021/om050790r CCC: $33.50
Publication on Web 08/08/2006

for the approach of the monomer to the metal and then to perform more accurate calculations on the stationary points. The PEC corresponds to a monodimensional section of the total potential energy hypersurface (PEH), with all but one of the geometrical variables relaxed.

Our active catalyst consisted of a $[Cp_2MCH_3]^+/CI_X^-$ complex, where M = Ti, Zr, or Hf and CI stands for counterion: $CI_{real}^- = [CH_3B(C_6F_5)_3]^-$ and $CI_{model}^- = [CH_3B(CF_2Cl)_3]^-$. The monomer was ethylene in all the calculations. We will refer to the moieties containing M = Ti as titanocenes (Tc), and similarly zirconocenes (Zc) and hafnocenes (Hc) for M = Zr and Hf, respectively.

We have performed three types of calculations throughout this work. First, relaxed PECs have been performed for the approach and insertion of a monomer unit into the growing chain attached to the zirconocenic catalyst. For these scans we chose the SKBJ effective core potential (ECP) basis set,[24−26] as defined in the Extensible Computational chemistry environment basis set database.[27] We chose this basis set for performance considerations, since it has all of the core electrons described by pseudopotential functions, and only the valence shell of each element is described with Gaussian basis functions, thus reducing the computational expense considerably. To better describe the anions, we have extended the SKBJ basis set adding a set of diffuse functions, consisting of S-type functions with an exponent one-third that of the previously most diffuse one for each element. We have called this basis set SKBJ+.

With regard to the theoretical method used, it is worth noting that the lack of a pruned grid for the Zr element for the computation of the spatial integrals in the DFT method leads to an enormous performance loss (through the use of unpruned grids). We have tried to overcome this by optimizing the $[Cp_2ZrCH_3]^+/CI_{real}^-$ species along the PEC at the HF/SKBJ+ level, then refining the final energy through a B3LYP/SKBJ+ single-point calculation. Thus B3LYP/SKBJ+//HF/SKBJ+ energies have been used to build up a PEC for $[Cp_2ZrCH_3]^+/CI_X^-$, where X = real and model, to compare the CI_{model}^- to CI_{real}^-, and then B3LYP/SKBJ+ energies for $[Cp_2ZrCH_3]^+/CI_{model}^-$ have also been taken from ref 16 to compare B3LYP//HF and full B3LYP PECs.

Second, geometry optimizations and subsequent frequency calculations have been carried out for the stationary points found in this zirconocene PEC and the titanocene and hafnocene counterparts (for the latter two, PEC calculations have not been performed). For these optimizations we have made use of the LanL2DZdp basis set, which is an extension of the LanL2DZ basis set,[28−30] supplemented with diffuse and polarization functions.[31] Unfortunately there is no such extension for boron, titanium, zirconium, or hafnium, so we have used the bare LanL2DZ basis set for these elements. The LanL2DZ basis set is a pseudopotential one, as it is SKBJ, but with a smaller core described with ECPs, so that an increase in accuracy is expected, at the expense of an actual increase in computational cost.

The LanL2DZdp optimizations and frequency calculations have all been performed at the B3LYP level, for reactant, complexation TS, monomer π-complex, insertion TS, and inserted product, for CI_{model} (and all three metals). All the frequency calculations have come up with real frequencies for all the normal modes of the local minima, and only one imaginary frequency (negative force constant) for the transition states. We have also confirmed that in every case the negative force constant corresponded to the desired normal mode.

Due to computational limitations, transition states have not have been optimized for CI_{real}, and only two optimized geometries incorporating CI_{real} have had their frequencies calculated. Although the LanL2DZdp optimizations could have been performed, performing frequency calculations (in order to make sure that only one vibrational mode with a negative force constant (imaginary frequency) and appropriate atomic motions was present), on all the structures would have been too expensive, and their lack would render the optimized TSs virtually useless. Minima have been accepted without frequency test, but we would not feel confident doing so with the TSs. The frequency calculations indeed performed, namely, for Zc_{reac}^{real} and Zc_{comp}^{real} (zirconocene with CI = CI_{real}, reactant, and π-complex, respectively), were carried out (at a great expense) in order to have at least one model versus real ΔG.

Third, single-point energy calculations have been done (on all the geometries previously optimized at the LanL2DZdp level) at the B3LYP/6-311++G(3df,3pd) level. This basis set is widely known and was used as implemented in Gaussian, for all the elements except for titanium, zirconium, and hafnium, for which the SDD basis set was used, as implemented in Gaussian. We have called this basis set TZ throughout the present work.

All the calculations have been carried out using the GAUSSIAN 98[32] and GAUSSIAN 03[33] packages, and the Hartree−Fock (HF) and B3LYP density functional (DFT) methods, as implemented therein.

For the ball-and-stick graphical representation of molecules, the Raster3D software[34] has been extensively used throughout this article. Various graphs and schematic figures have been produced with Grace,[35] Xfig,[36] and ChemTool.[37]

3. Results and Discussion

3.1. PEC Scan. Relaxed potential energy surface scans have been performed for $[Cp_2ZrCH_3]^+/CI_X^-$, X = real and model. These scans are equivalent to those performed elsewhere,[16] but with a less expensive HF/SKBJ+ optimization, followed by a B3LYP/SKBJ+ single point on each optimized geometry. As in that article, we have scanned the Zr−C_1C_2 distance, meaning a fixed (and equal) Zr−C distance for both carbon atoms of the incoming ethylene monomer. All other variables were relaxed (optimized) at each Zr−C_1C_2 point. The C_2-C_α distance has also been used as a pseudo-reaction coordinate in an additional PEC scan. Recall that C_α designates the carbon atom

(24) Stevens, W. J.; Basch, H.; Krauss, M. *J. Chem. Phys.* **1984**, *81*, 6026.

(25) Stevens, W. J.; Krauss, M.; Bausch, H.; Jasien, P. G. *Can. J. Chem.* **1992**, *70*, 612.

(26) Cundari, T. R.; Stevens, W. J. *J. Chem. Phys.* **1993**, *98*, 5555.

(27) Basis sets were obtained from the Extensible Computational Chemistry Environment Basis Set Database, Version 02/25/04, as developed and distributed by the Molecular Science Computing Facility, Environmental and Molecular Sciences Laboratory, which is part of the Pacific Northwest Laboratory, P.O. Box 999, Richland, WA 99352, and funded by the U.S. Department of Energy. The Pacific Northwest Laboratory is a multiprogram laboratory operated by Battelle Memorial Institute for the U.S. Department of Energy under contract DE-AC06-76RLO 1830. Contact David Feller or Karen Schuchardt for further information.

(28) Dunning, D. H., Jr.; Hay, P. J. In *Methods of Electronic Structure Theory, Vol. 2*; Schaefer, H. F., III, Ed.; Plenum Press: New York, 1977.

(29) Hay, P. J.; Wadt, W. R. *J. Chem. Phys.* **1985**, *82*, 270.

(30) Ortiz, J. V.; Hay, P. J.; Martin, R. L. *J. Am. Chem. Soc.* **1992**, *114*, 2736.

(31) Check, C. E.; Faust, T. O.; Bailey, J. M.; Wright, B. J.; Gilbert, T. M.; Sunderlin, L. S. *J. Phys. Chem. A* **2001**, *105*, 8111.

(32) Frisch, M. J.; et al. *Gaussian 98*, revision a.11.3; Gaussian, Inc.: Pittsburgh, PA, 2002.

(33) Frisch, M. J.; et al. *Gaussian 03*, revision c.02; Gaussian, Inc.: Wallingford, CT, 2004.

(34) Merrit, E. A.; Bacon, D. J. *Methods Enzymol.* **1997**, *277*, 505. *Raster3D* can be freely downloaded at: http://www.bmsc.washington.edu/raster3d/.

(35) *Grace 5.1.18*. Downloadable under the GPL license at: http://plasma-gate.weizmann.ac.il/Grace/.

(36) Sutanthavibul, S.; Yap, K.; Smith, B. V.; King, P.; Boyter, B.; Sato, T. *Xfig 3.2.5*. Freely downloadable at: http://www.xfig.org/, 1985−2005.

(37) Kroeker, M.; Liboska, R.; Banck, M.; Volk, T. *Chemtool 1.6.7*. Downloadable under the GPL license at: http://ruby.chemie.uni-freiburg.de/martin/chemtool/chemtool.html.

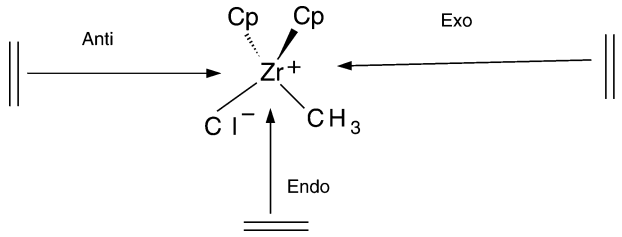

Figure 1. Three possible monomer approach paths for the considered metallocenic catalyst.

of the methyl group bound to the metal cation in the reactant. Similarly, C_1 designates the carbon, belonging to the incoming monomer, that will bind to the zirconium cation in the product, and C_2 designates the carbon atom of the monomer that will bind to C_α. Recall that the reference energy for calculating the ΔE's (the *Y*-axis values of the PECs) has been taken as the sum of those of infinitely separated ethylene and $[Cp_2ZrCH_3]^+/CI_X^-$ (X = real and model, respectively).

The present work, however, considers two possible monomer approach paths, which the previous article[16] did not. A careful inspection of the catalyst geometry shows that there are three possible paths, as depicted in Figure 1. Our previous article featured the "Exo" path, and here we consider all three of them.

Two regions have been distinguished in each scan. Figure 2 depicts them for the Exo approach to $[Cp_2ZrCH_3]^+/CI_{model}^-$. A description of these scans follows. Notice that the qualitative structure of these PECs was identical for both CI_{model} and CI_{real} in the Exo and also the other two approach paths and is expected to be equal for the other two metals (Ti and Hf).

In the $Zr-C_1C_2$ scan (right-hand side of Figure 2), as the monomer approaches the metal from $d(Zr-C_1C_2) = 6.0$ to 3.7 Å, a monotonically increasing energy profile is found. This region has been fitted to a Gaussian function (eq 1). In the same scan, as the monomer gets still closer, a complexation basin is observed for $d(Zr-C_1C_2) = 3.6$ to 2.5 Å. Here the monomer has displaced the counterion in the coordination sphere of the metal. This region has been fitted to a Morse-type function (eq 2) and corresponds to the π-complex intermediate. These two regions are differentiated because, whereas in the monomer approach curve, the CI is still closely bound to the metal cation, in the complexation basin the CI has been displaced. The $d(Zr-C_{CI})$ versus $d(Zr-C_1C_2)$ curve is given in the Supporting Information.

The next step of this reaction consists in the formation of the C_2-C_α bond. The corresponding scan is depicted on the left-hand side of Figure 2. In that scan a transition region can be assigned to $d(C_2-C_\alpha) = 3.0$ to 1.8 Å, which has been fitted to a third-order polynomial. This region is characterized by a long $Zr-C_{CI}$ distance (displaced counterion) and a short $Zr-C_\alpha$ distance (α-carbon still bound to the metal).

For closer C_2-C_α distances a C−C bond formation region is found (which corresponds to the insertion product). This region is characterized by a short $Zr-C_{CI}$ distance (counterion takes its place in the Zr coordination sphere back) and a long $Zr-C_\alpha$ distance (α-carbon jumps to a γ-position, once the monomer has inserted its two carbons between it and the metal). The $d(Zr-C_{CI})$ and $d(Zr-C_\alpha)$ versus $d(C_2-C_\alpha)$ plot is given in the Supporting Information. This region has been also fitted to a Morse-type potential. The parameters for these fits can be found in the Supporting Information.

For CI_{real}, the four regions are quite similar. The features of the regions we identify in them are similar to those of the CI_{model} ones (Figure 2). The curves can be fitted to the corresponding model functions, and the fitted parameters are also provided in the Supporting Information.

$$V_{Gauss} = \alpha + \beta e^{-\gamma(x-\delta)^2} \quad (1)$$

$$V_{Morse} = A + B(1 - e^{-C(x-D)})^2 \quad (2)$$

To be able to assess the reliability of our CI_{model} compared to CI_{real}, the four fitted functions have been used. With each one of them we have defined a difference ϵ as the square root of the average square of the difference between the fitted function for CI_{real} and the one for CI_{model} (see eq 3).

$$\epsilon_{\alpha|\beta}^2 = \frac{1}{x_2 - x_1}\int_{x_1}^{x_2}(V_\alpha(x) - V_\beta(x))^2\,dx \quad (3)$$

The values of the differences so defined are given in Table 1.

It is apparent from Table 1 that the discrepancy between the results obtained with the model CI and the real one (both at the B3LYP//HF level) is close to, and in some cases even within, chemical accuracy (less than 1 kcal/mol).

Additionally, approximate stationary points have been extracted from the fitted functions, in the following manner: the

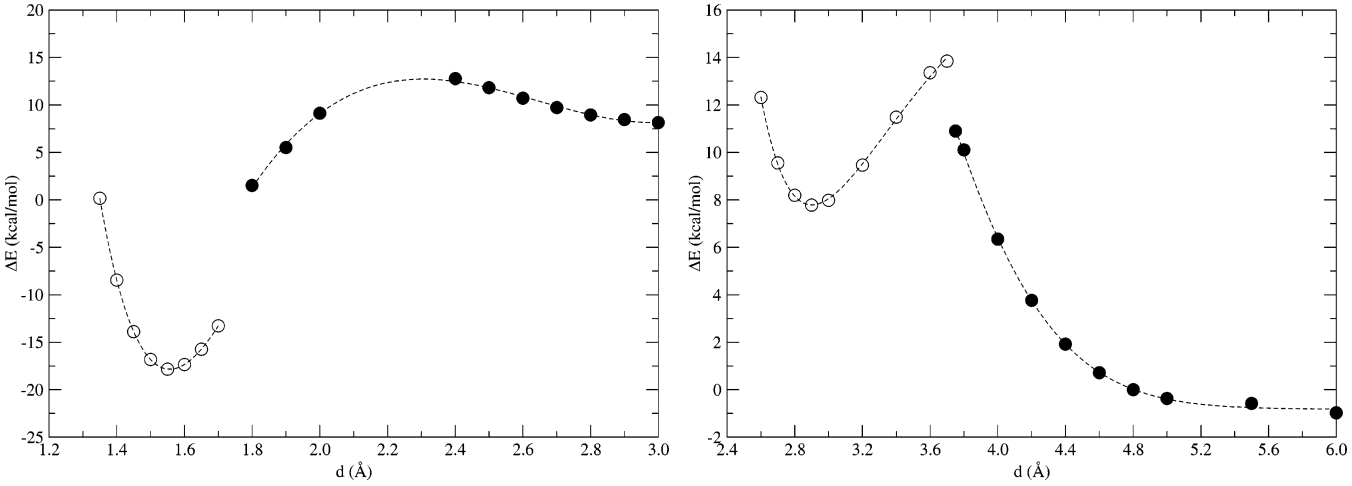

Figure 2. PEC corresponding to varying the C_2-C_α (left) and $Zr-C_1C_2$ (right) distances for the Et + $[Cp_2ZrCH_3]^+/CI_{model}^-$ system at the B3LYP//HF level. In each plot white and solid black circles have been used to distinguish the two surfaces (see text), and the corresponding fitted functions are represented by dashed lines. Distances in Å and energies in kcal/mol.

Table 1. Energetic Differences (kcal/mol) Defined in Eq 3 for the Model/Real CI PEC Comparisons

region	Exo	Anti	Endo
ZrCC basin	1.84	0.86	0.51
ZrCC approach	1.74	0.48	0.43
CC basin	0.11	0.11	0.11
CC approach	2.14		0.73

Table 2. ΔE Values (kcal/mol) for the Reaction Stationary Points, as Obtained from the Exo PEC Scans for $[Cp_2ZrCH_3]^+/CI^-_{model}$

	CI_{model}			CI_{real}		
	Exo	Anti	Endo	Exo	Anti	Endo
TS1	13.0	10.9	5.9	15.2	9.2	9.2
π-complex	7.6	5.5	0.2	9.0	5.8	0.4
TS2	12.4		12.5	14.4	13.1	12.5
product	−18.7			−18.5		

Table 3. Geometric Parameters for the Reaction Stationary Points, as Obtained from the PEC Scans for $[Cp_2ZrCH_3]^+/CI^-_X$, X = Model and Real[a]

	CI_{model}			CI_{real}		
	Exo	Anti	Endo	Exo	Anti	Endo
TS1	3.63	3.41	3.43	3.55	3.42	3.60
π-complex	2.90	2.86	2.84	2.83	2.87	2.83
TS2	2.31		2.17	2.33	2.28	2.15
product	1.56			1.56		

[a] The presented values correspond to $d(Zr-C_1C_2)$ for TS1 and π-complex and $d(C_2-C_\alpha)$ for TS2 and product. All distances in Å.

complexation TS (TS1) has been taken as the calculated crossing point of the V_{Gauss} of the ZrCC approach zone and the V_{Morse} of the ZrCC basin; the π-complex corresponds to the minimum of the V_{Morse} of the ZrCC basin; the insertion TS (TS2) is the maximum in the third-grade polynomial of the CC approach zone; and the product is identified with the minimum in the V_{Morse} of the CC basin. The values obtained for the energies are given in Table 2, and the geometrical parameters in Table 3. The values for Anti and Endo paths are not given in Tables 2 and 3 because the C−C bond formation basin has been taken as identical for all three paths (see above). The values for the Anti TS2 could not be obtained for $CI = CI_{model}$, due to technical limitations. This TS has a particularly long $Zr-C_{CI}$ distance, and our model tended to turn around and bind through a fluorine atom.

It is worth noting the fact that we have considered the CC basins (and thus the reaction products) to be the same for all three paths. The rationale behind this is as follows: the counterion is quite separated from the central metal in the insertion TSs (TS2), and it takes back its position in the coordination sphere of the metal quite easily after the C−C bond has been formed.[8] Upon visual inspection of the geometries of the Endo and Anti TS2 structures, it is apparent that in both cases the CI will go to the same place in the product. In addition, the Exo product is also equivalent to the Endo/Anti one, because what separates them is a rotation of the growing chain around the $Zr-C_\alpha$ bond. The energetic profile for that rotation is given in Figure 3. Inspection of that figure shows that, although the three maxima (and minima) do not have the same height and are not exactly equally spaced, they are close to indeed being. It is also evident that transition from any minimum to any other one requires a single jump over a barrier of around 3.5 kcal/mol. This rotation barrier is not negligible, but since the propagation reaction barrier is much higher (on the order of 20−30 kcal/mol) and the three rotation minima are close to degeneracy, it can be assumed that the product will distribute equally among the three states much faster than the next polymerization reaction step.

3.1.1. Reaction Rate Order from the PECs. It is evident that we face a two-step reaction, with a high barrier for the (forward) first step and a low one for both the forward second step and the backward first step. The backward second step will be dismissed. This reaction, hence, can be given in short chemical notation as eq 4.

$$\mathrm{Et} + \mathrm{Catalyst} \underset{k_{-1}}{\overset{k_1}{\rightleftharpoons}} \mathrm{Complex} \xrightarrow{k_2} \mathrm{Product} \tag{4}$$

According to eq 4, and applying the stationary-state approximation, we have eq 5:

$$0 \approx \frac{\mathrm{d[Complex]}}{\mathrm{d}t} = k_1[\mathrm{Et}][\mathrm{Catalyst}] - k_{-1}[\mathrm{Complex}] - k_2[\mathrm{Complex}] \tag{5}$$

Since, by definition, $k_2[\mathrm{Complex}] = \mathrm{d[Product]}/\mathrm{d}t$, minimal algebra gives eq 6.

$$\frac{\mathrm{d[Product]}}{\mathrm{d}t} = \frac{k_1 k_2}{k_{-1} + k_2}[\mathrm{Et}][\mathrm{Catalyst}] \tag{6}$$

Equation 6 shows that, under the proposed conditions, the propagation reaction rate is a bimolecular one and that a global $k_T = k_1k_2/(k_{-1} + k_2)$ can be calculated. If we assume that $k_x = A \exp(-\Delta G_x/RT)$, and for pre-exponential factors that cancel out, it turns out that one can calculate a global reaction Gibbs free energy from the individual ΔG's of each step, as given by eq 7.

$$\Delta G_T = \Delta G_1 + \Delta G_2 + RT \ln(e^{-\Delta G_{-1}/RT} + e^{-\Delta G_2/RT}) \tag{7}$$

We will use eq 7 in the following section, where we calculate Gibbs free energies. However, up to this point, we have calculated only potential energy profiles. Substituting Gibbs free energies for electronic energies in that equation, we could find an estimate of the global ΔE's that these scans predict for the three monomer approach paths, in the cases of CI_{model} and CI_{real}, for the zirconocene. These "global" ΔE's are given in Table 4, using a RT value of 0.596 kcal/mol ($T = 300$ K).

3.2. Stationary Points. We picked the stationary points of the PEC scans and optimized their geometries with the LanL2DZdp basis set: the maximum (complexation TS) and minimum (π-complex) of the $d(Zr-C_1C_2)$ scan and the maximum (insertion TS) and minimum (product) of the $d(C_2-C_\alpha)$ scan, as well as the ethylene and metallocene moieties infinitely separated (reactants), and their energies were refined by means of single-point energy calculations with the TZ basis set. This procedure was followed for the three monomer approach paths. All the stationary points were calculated for $CI = CI_{model}$, and only local minima for $CI = CI_{real}$.

The geometries and the energy (PEC) and free energy (FEC) profiles for the Exo approach to $[Cp_2ZrCH_3]^+/CI^-_{model}$ are depicted in Figure 4, along with the (parenthesized) energies for $CI = CI_{real}$. For brevity's sake, PECs and FECs for Endo and Anti approaches to zirconocene and those of titanocene and hafniocene are omitted.

The model/real counterion energetic discrepancies are depicted in Figure 5. As can be seen, the differences are small in general, only seldom rising slightly over chemical accuracy values (1 kcal/mol). Additionally the one $\Delta\Delta G$ calculated,

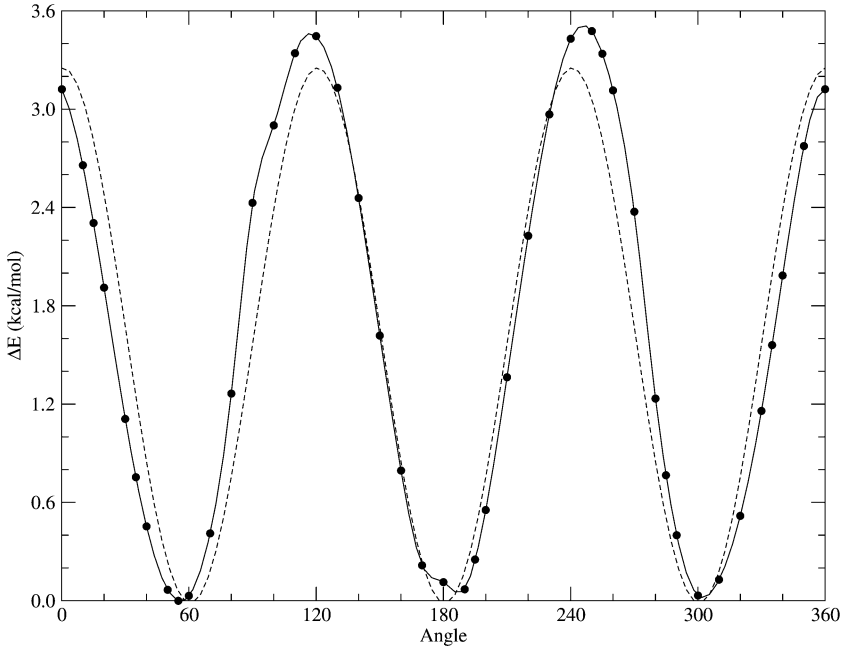

Figure 3. Energy profile for the rotation, along the $Zr-C_\alpha$ bond, of the growing chain R in $[Cp_2ZrR]^+/CI^-_{model}$, where R = propyl. The solid line corresponds to a cubic spline, and the dashed line to a simple period-three cosine fit.

Table 4. Global Reaction Energy Barriers for the Propagation Step of Ethylene Polymerization through an Exo Monomer Approach Path, as Calculated from Eq 7 with Values Taken from PEC Scans[a]

path	CI_{model}	CI_{real}
Exo	12.4	14.4
Anti		13.1
Endo	12.5	12.5

[a] Recall that we are using energies, and not free energies. All values in kcal/mol.

namely, $\Delta\Delta G = \Delta G(Zc^{model}_{comp}) - \Delta G(Zc^{real}_{comp})$, gives a discrepancy of only 0.32 kcal/mol.

All the electronic energies are summarized in Table 5, and the Gibbs free energies in Table 6.

It is worth mentioning that the Tc^{model}_{TS1} is slightly lower than Tc^{model}_{comp} in the Exo FEC. This is no paradox, of course, because it is indeed higher in the electronic energy surface, and that is the space where the geometry optimization calculations take place. However, the energy corrections obtained from the frequency calculations raise the π-complex more than they do the TS, and hence it looks like the structure that is a TS in the PES is not so in the Gibbs free energy surface (FES). Unfortunately, it is not presently feasible to optimize directly in the FES.

To have more compact numbers to quantify differences, we can resort to eq 7. Assuming an example *RT* of 0.576 kcal/mol ($T = 300$ K), we come up with the global ΔG values tabulated in Table 7.

We can compare the energies on the right-hand side of Table 7 with those in Table 4, as well as geometrical parameters in Table 8 with those in Table 3, to assess the accuracy of the B3LYP/SKBJ+//HF/SKBJ+ scans, with respect to the B3LYP/TZ//B3LYP/LanL2DZdp optimizations. All we can conclude is that the SKBJ+ energies seem to be underestimated by around 7 kcal/mol. However, when it comes to geometry, the concordance is not that bad, at least for local minima. SKBJ+ scans correctly predict a longer Exo TS1 $d(Zr-C_1C_2)$ and TS2 $d(C_2-C_\alpha)$, but greatly overestimate the $d(Zr-C_1C_2)$ of all TS1's. For the π-complex, the SKBJ+ $Zr-C_1C_2$ distances seem to be quite accurate, if only a bit underestimated for $CI = CI_{real}$. The product C_2-C_α distances do not change much from the scans to the optimizations.

Regarding a prediction of a preferred path for each metal, looking at Table 7 it seems that both Exo and Anti approach paths have almost the same free energy barrier for each metal, whereas the Endo approach path is always unfavorable. Take into account that for our achiral catalyst, and ethylene as monomer, all the paths lead to equivalent products. This might not be the case for other polymerizing systems, where one path might be greatly favored over the others. Particularly, when an alternating monomer complexation site (growing chain swinging) is required to explain the experimentally obtained tacticity, it seems intuitive that the Exo path should be the preferential one.

On the other hand, if we compare the metals among them, we observe that the heavier metals have higher overall reaction barriers. This can be tracked back to the binding energies (BE) of the counterions (eq 8).

$$[Cp_2MCH_3]^+/[CH_3B(CF_2Cl)_3]^- \rightarrow [Cp_2MCH_3]^+ + [CH_3B(CF_2Cl)_3]^- \quad (8)$$

The values of these BEs (see Table 9) indicate a clearly less tightly bound CI for M = Ti (by around 10 kcal/mol) and similar tightness for M = Zr and Hf (within 1 kcal/mol). This seems to imply that, as expected, the stronger the metal/CI bond, the harder for the monomer to displace the latter and form the π-complex; moreover, our data also show a similar correlation for the insertion barrier, for reasons still unclear.

It may come as a surprise that for this system the activity of the M = Ti case would be higher than that of Zr and Hf (because the complexation and insertion barriers are lower). There is, indeed, literature regarding zirconium as the most active metal of the three, followed by hafnium, and titanium at a far third position.[3] Other comparisons between Ti and Zr germanium-

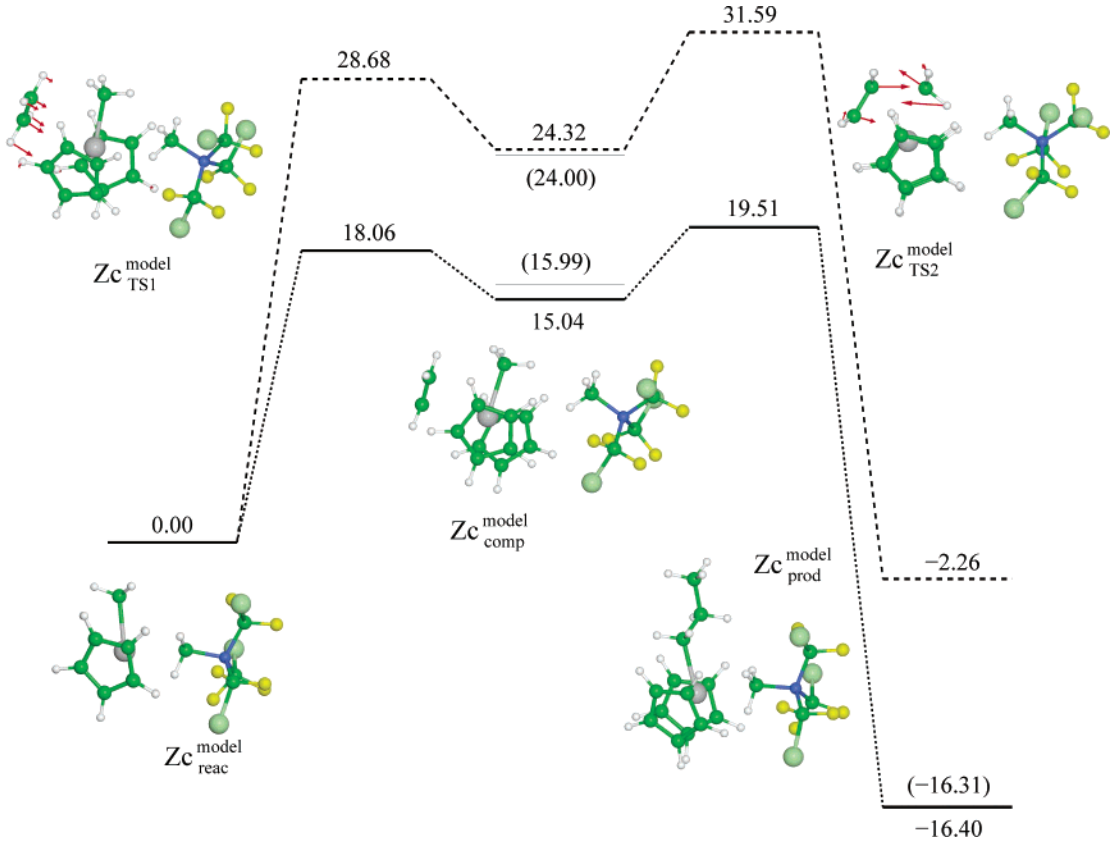

Figure 4. Stationary points along the Et + $[CH_3ZrCp_2]^+/Cl^-_{model}$ reaction PECs. Solid lines correspond to electronic energies, and dashed lines to Gibbs free energies, both values in kcal/mol at the B3LYP/TZ//B3LYP/LanL2DZdp level. The values for CI = CI_{real} are given in parentheses. The arrows in Zc^{model}_{TS1} and Zc^{model}_{TS2} correspond to the motion of the atoms according to the normal mode with a negative force constant. The scale is arbitrary, but the ratios of the moduli of the vectors match the atomic displacement ratios in that mode.

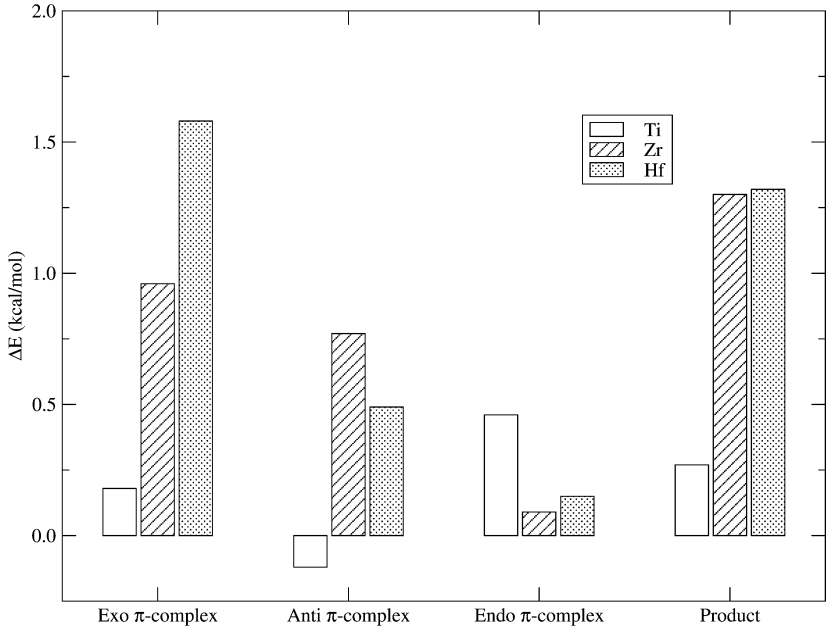

Figure 5. Energy differences between species calculated with real and model counterions. Values in kcal/mol.

bridged *ansa*-metallocenes[17] regard Zr as around twice as active as Ti toward ethylene and propylene polymerization. Beckerle et al.[18] studied some post-metallocenic bisphenolic compounds of the type $[\{S(CH_2)_2S\}(OC_6H_2\text{-}^tBu_2\text{-}4,6)_2MX_2]$ and found that for M = Ti, Hf the activity toward styrene polymerization was similar (with Hf slightly more active), and M = Zr was clearly more active than any of the former two. Theoretical studies by Vanka et al. on a nitrogenated post-metallocene[10] also come up with a lower barrier for the polymerization by zirconium than by titanium.

However, the data on the subject are far from uncontroversial, since recent works by Bott et al.[19] report similar activities for

Table 5. Summary of Electronic Energies of Stationary Points in the $[Cp_2MCH_3]^+/CI_X^-$ + Ethylene Reaction Potential Energy Curves (PECs), M = Ti, Zr, and Hf, and X = Model and Real

		CI_{model}				CI_{real}	
metal	path	TS1	π-complex	TS2	product	π-complex	product
Ti	Exo	13.39	11.59	14.42	−16.24	11.77	−15.78
	Anti	18.10	11.42	14.89	−16.24	11.68	−15.78
	Endo	13.80	7.63	17.12	−16.24	7.52	−15.78
Zr	Exo	18.06	15.04	19.51	−16.40	15.99	−16.31
	Anti	16.21	12.67	18.84	−16.40	13.97	−16.31
	Endo	9.53	7.46	20.96	−16.40	8.23	−16.31
Hf	Exo	18.51	15.40	21.15	−16.23	16.99	−16.07
	Anti	18.20	13.10	21.33	−16.23	14.42	−16.07
	Endo	11.33	8.03	22.60	−16.23	8.52	−16.07

Table 6. Summary of Gibbs Free Energies of Stationary Points in the $[Cp_2MCH_3]^+/CI_{model}^-$ + Ethylene Reaction Potential Energy Surfaces (PESs), M = Ti, Zr, and Hf, and X = Model[a]

metal	path	TS1	π-complex	TS2	product
Ti	Exo	20.55	21.52	26.46	0.16
	Anti	27.65	21.29	26.07	0.16
	Endo	23.89	19.57	29.91	0.16
Zr	Exo	28.68	24.32	31.59	−2.26
	Anti	29.57	21.84	31.82	−2.26
	Endo	22.81	18.59	33.91	−2.26
Hf	Exo	29.08	25.27	32.96	−2.49
	Anti	31.67	22.40	32.45	−2.49
	Endo	24.61	18.97	35.49	−2.49

[a] The π-complex ΔG value for the Exo approach to $[Cp_2ZrCH_3]^+/CI_{real}^-$ is 24.00 kcal/mol. All values in kcal/mol.

Table 7. Global Propagation Reaction Gibbs Free Energy Barriers (left), as Obtained from Data in Table 6 and Eq 7, and Global Electronic Energy Barriers (right), for Comparison Purposes with Data in Table 4[a]

	ΔG			ΔE		
	Exo	Anti	Endo	Exo	Anti	Endo
Ti	26.46	27.69	29.91	14.52	18.10	17.12
Zr	31.60	31.84	33.91	19.56	18.85	20.96
Hf	32.96	32.60	35.49	21.85	21.33	22.60

[a] All values in kcal/mol.

Table 8. Geometric Parameters for the Reaction Stationary Points, as Optimized for $[Cp_2ZrCH_3]^+/CI_X^-$, X = Model and Real[a]

	CI_{model}			CI_{real}		
	Exo	Anti	Endo	Exo	Anti	Endo
TS1	3.394	3.080	3.296			
π-complex	2.896	2.841	2.857	2.924	2.981	2.845
TS2	2.229	2.215	2.117			
product	1.539			1.539		

[a] The presented values correspond to $d(Zr-C_1C_2)$ for TS1 and π-complex and $d(C_2-C_\alpha)$ for TS2 and product. All distances in Å.

Ti- and Zr-bearing monocyclopentadienyl phenoxy-imines and -amines, as well as for Cp_2MCl_2/MAO, M = Ti and Zr. Even more recent studies by Gil and Casagrande[20] on exotic hydrotris(pyrazolyl)borateMCl_3 derivatives conclude that, depending on some substituents, Ti can have slightly more or slightly less activity than Zr toward ethylene polymerization.

However, some metallocenic catalysts show outright higher activity for the titanated system than for the zirconated one, e.g., some β-diketiminato complexes.[21] Early work by Kaminsky[22] regards Ti as more active than Zr, but reckon a decrease in titanium activity caused by its reduction from Ti(IV) to Ti(III), which is inactive for polymerization. This deactivation through reduction is observed to increase as the reaction temperature increases.[5] Kaminsky also discusses a propylene polymerization case where hafnium is approximately 3 times less active than zirconium. The decrease in polymerization activity as temperature increases, for Ti(IV) compounds, is also observed by Lee et al.[38] Kim et al. are also "surprised"[23] that for their silacycloalkane-bridged *ansa*-metallocenes the activity of the titanated complexes is indeed higher than that of the zirconated ones, by almost an order of magnitude in some cases.

Table 9. Counterion Binding Energies for M = Ti, Zr, and Hf[a]

M	BE (CI_{model})	BE (CI_{real})
Ti	−74.33	−71.47
Zr	−83.55	−81.21
Hf	−84.48	−82.08

[a] Electronic energies calculated at the B3LYP/TZ//B3LYP/LanL2DZdp theory level.

It is of great interest the fact that titanium complexes have been reported to have a decreased activity when increasing the reaction temperature. This means that there are competitive deactivating processes, e.g., the reduction to Ti(III) mentioned above, but also that these processes are more sensitive to temperature changes than the propagation step itself is, because *both* polymer chain growth and deactivation must a priori be accelerated when increasing the temperature, but the latter accelerates more, resulting in an overall activity decrease.

Our results so far predict a lower barrier for the titanated metallocene, which rationalizes fairly well the experimentally observed[5,22,23,38] high activity at low temperatures, and small temperature sensitivity of the base reaction rate constant. The latter is inferred from the observed decrease of the overall reaction rate at higher temperatures, where the thermal deactivation of Ti(IV) to Ti(III) takes over.

4. Conclusions

The substitution of Zr by group 4 Ti and Hf transition metals as the active center in metallocene-catalyzed olefin polymerization has been analyzed. The monomer complexation and insertion barriers are found to be lower for titanium than for its heavier counterparts. This, although not a ubiquitous trend in metallocenic and post-metallocenic catalysts, is in good agreement with the superior activity for Ti at lower temperatures, found at least in some titanocenes.

We have also tested three possible reaction paths and found that the ones where the monomer approaches the metal from behind the growing chain attached to it (Exo approach) and from behind the counterion (Anti) are significantly favored over the path where the monomer approaches the metal from between the counterion and the growing chain (Endo).

It is also apparent from the results obtained that $[CH_3B(CF_2Cl)_3]^-$ is indeed a convenient and accurate replacement for $[CH_3B(C_6F_5)_3]^-$ in quantum mechanical calculations of metallocene-catalyzed olefin polymerizations.

The energetic differences when sketching a PEC at the B3LYP/SKBJ//HF/SKBJ theory level are close to chemical accuracy. Although the error introduced by not considering electron correlation in the optimization (see Table 1) is small in general, in the C−C bond formation zone it seems to go

(38) Lee, M. H.; Han, Y.; Kim, D.-H.; Hwang, J.-W.; Do, Y. *Organometallics* **2003**, *22*, 2790.

above 2.5 kcal/mol. On the other hand, the error introduced by substituting CI_{real} by CI_{model} is consistently small, and below 1.5 kcal/mol for the four regions depicted in Figure 2.

The model/real CI energetic discrepancies are even smaller in the case of the B3LYP/LanL2DZdp stationary points, where they are all around the chemical accuracy threshold.

Acknowledgment. This research was funded by Euskal Herriko Unibertsitatea (the University of the Basque Country), Gipuzkoako Foru Aldundia (the Provincial Government of Gipuzkoa), and Eusko Jaurlaritza (the Basque Government). The SGI/IZO-SGIker UPV/EHU (supported by Fondo Social Europeo and MCyT) is gratefully acknowledged for generous allocation of computational resources.

Supporting Information Available: Plots of some interatomic distances, parameter values for fitting functions, and full text of refs 32 and 33. This material is available free of charge via the Internet at http://pubs.acs.org.

OM050790R